nature physics

Article

https://doi.org/10.1038/s41567-023-02345-4

False vacuum decay via bubble formation in ferromagnetic superfluids

Received: 22 May 2023

Accepted: 16 November 2023

Published online: 22 January 2024

Check for updates

A. Zenesini[1,2] ✉, A. Berti[1], R. Cominotti[1], C. Rogora[1], I. G. Moss[3], T. P. Billam[4], I. Carusotto[1], G. Lamporesi[1,2] ✉, A. Recati[1] ✉ & G. Ferrari[1,2]

Metastability stems from the finite lifetime of a state when a lower-energy configuration is available but only by tunnelling through an energy barrier. It is observed in many natural situations, including in chemical processes and in electron field ionization. In classical many-body systems, metastability naturally emerges in the presence of a first-order phase transition. A prototypical example is a supercooled vapour. The extension to quantum field theory and quantum many-body systems has attracted significant interest in the context of statistical physics, protein folding and cosmology, for which thermal and quantum fluctuations are expected to trigger the transition from the metastable state (false vacuum) to the ground state (true vacuum) through the probabilistic nucleation of spatially localized bubbles. However, the long-standing theoretical progress in estimating the relaxation rate of the metastable field through bubble nucleation has not been validated experimentally. Here we experimentally observe bubble nucleation in isolated and coherently coupled atomic superfluids, and we support our observations with numerical simulations. The agreement between our observations and an analytic formula based on instanton theory confirms our physical understanding of the decay process and promotes coherently coupled atomic superfluids as an ideal platform to investigate out-of-equilibrium quantum field phenomena.

A supercooled gas is a classic example of a metastable state that exists just across a first-order phase transition. The passage to the ground state (the liquid phase) is mediated by resonant bubble nucleation when the energy gain provided by the liquid bulk is compensated by the cost of the surface tension. This energy balance leads to a critical bubble size. The stochastic formation of a bubble typically occurs around nucleation spots, such as impurities in the gas or imperfections of the container. The extension of this idea to a quantum many-body or a quantum field system has attracted extensive attention in a wide range of scenarios and length scales, from an understanding of the early Universe[1–3] to the characterization of spin chains[4–6] and protein folding[7,8]. In all these models, the metastable state at the origin of bubble nucleation is identified as 'false vacuum' (FV), and the role of surface tension is taken by a genuinely quantum term. In the purest form, the decay of the FV into the ground state takes place through quantum vacuum fluctuations[9,10] (like impurities in the classical case). However, as, for example, in the early Universe, the tunnelling is equally likely to be boosted by thermal fluctuations, and the process is styled vacuum decay at finite temperature[11] (see refs. 12–14 for reviews).

[1]Pitaevskii BEC Center, CNR-INO and Dipartimento di Fisica, Università di Trento, Trento, Italy. [2]Trento Institute for Fundamental Physics and Applications, INFN, Trento, Italy. [3]School of Mathematics, Statistics and Physics, Newcastle University, Newcastle upon Tyne, UK. [4]Joint Quantum Centre (JQC) Durham–Newcastle, School of Mathematics, Statistics and Physics, Newcastle University, Newcastle upon Tyne, UK. ✉e-mail: alessandro.zenesini@ino.cnr.it; giacomo.lamporesi@ino.cnr.it; alessio.recati@ino.cnr.it

https://doi.org/10.1038/s41567-023-02345-4

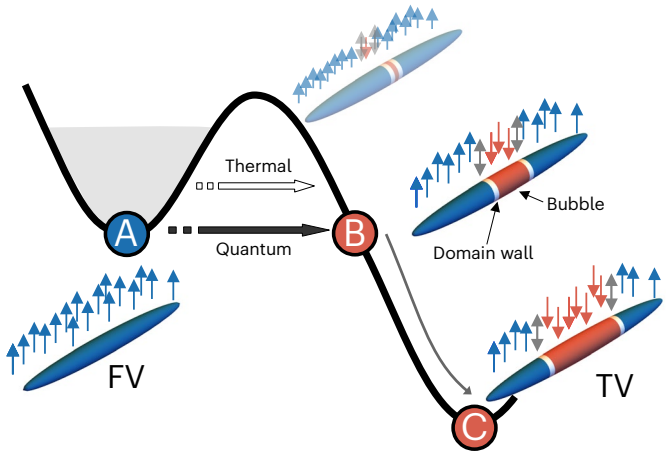

Fig. 1 | Mean-field energy and bubble formation. The cloud is initially prepared in the FV with all the atoms in $|\uparrow\rangle$ (A). Although the single $|\downarrow\rangle$ spin state is energetically lower ($E_\downarrow < E_\uparrow$) in the centre of the cloud, the situation is the opposite in the low-density tails. The interface (domain wall) between ferromagnetic regions with opposite magnetization has positive (kinetic) energy, which adds up to the double minimum energy landscape emerging from the ferromagnetic interaction. Macroscopic tunnelling can take place resonantly to the bubble state (B), which has a $|\downarrow\rangle$ bubble in the centre. The core energy gain compensates for the domain-wall energy cost. The barrier crossing can be triggered by quantum fluctuations in the zero-temperature case (full arrow) or by thermal fluctuations at finite temperature (empty arrow). After the tunnelling process, the bubble increases in size in the presence of dissipation to reach the true vacuum (TV) state (C), without coming back to (A).

In the cosmological case, the energy scales are well above any that are accessible to experiments, so that FV decay remains one of the most important yet untested processes in theoretical high-energy physics. Recently, the extreme flexibility of tabletop experiments with neutral and charged atoms and the advances in classical and quantum computer algorithms have paved the way for experiments[15–22] and virtual simulators[23,24]. Up to now, only numerical results have been achieved, and the experimental observation of an analogue to FV decay would, therefore, be of high relevance.

In tabletop experiments, an observation of bubble nucleation requires several ingredients that are difficult to arrange simultaneously. First, a mean-field interaction-induced energy landscape composed of an asymmetric double well is the minimal requirement for the decay from the metastable state to the absolute ground state through macroscopic tunnelling across the energy barrier followed by relaxation (Fig. 1). Second, unlike in the ordinary quantum tunnelling of a single particle[25–27], the system is described by a spatially dependent macroscopic field which can decay at the cost of the bubble surface energy. Third, the time resolution of the experiment should cover many orders of magnitude to allow for the investigation of the predicted exponential time-dependence of the tuning parameters, implying the need for high stability and accuracy. An extended ferromagnetic superfluid[28] possesses the ideal properties to act as a simulator of these field phenomena, thanks in particular to a first-order phase transition, its long-range coherence and the flexibility in controlling the experimental parameters within a stable and isolated environment. As a peculiarity of superfluids, spatial changes of the magnetization require a positive kinetic energy cost. In a tight analogy with supercooling, bubbles can, therefore, form in the ferromagnetic superfluid when the energy cost for creating their interfaces (domain walls) is balanced by the energy gain associated with the magnetization change inside the bubble (Fig. 1).

In this Article, we present the experimental observation of an FV decay process through bubble formation in a superfluid system. We observe that the duration of bubble nucleation scales exponentially with an experimental parameter that is connected to the energy barrier properties. Theoretical and numerical simulations support our observations and allow us to confirm the FV decay mechanism and its thermal activation.

The experimental platform is composed of a bosonic gas of ^{23}Na atoms, optically trapped and cooled below the condensation temperature. The gas is initially prepared in the internal state $|F, m_F\rangle = |2, -2\rangle = |\uparrow\rangle$, where F is the total angular momentum and m_F its projection on the quantization axis. Microwave radiation with amplitude Ω_R introduces coherent Rabi coupling between the $|\uparrow\rangle$ state and $|1, -1\rangle = |\downarrow\rangle$. The relevant scattering lengths for such a two-level system are $a_{\downarrow\downarrow} = 54.5a_0$, $a_{\uparrow\uparrow} = 64.3a_0$ and $a_{\downarrow\uparrow} = 64.3a_0$, and lead to the condition $\Delta a = (a_{\uparrow\uparrow} + a_{\downarrow\downarrow})/2 - a_{\downarrow\uparrow} < 0$, that is, to a system with a ferromagnetic ground state[28].

The trapping potential is axially symmetric and harmonic in all three directions, but strongly asymmetric (with axial and radial trapping frequencies $\omega_x/2\pi = 20$ Hz and $\omega_\rho/2\pi = 2$ kHz), producing an elongated system with inhomogeneous density and spatial size given by the longitudinal and radial Thomas–Fermi radii $R_x = 200$ μm and $R_\rho = 2$ μm. At the end of each experimental realization, we image the two spin states independently with two subsequent absorption imaging sequences[28] and extract their density distributions. The transverse confinement is tight enough to suppress the radial spin dynamics of the condensate[29]. We, therefore, integrate each image along the transverse direction and obtain the integrated one-dimensional (1D) density profiles $n_\uparrow(x)$ and $n_\downarrow(x)$, from which we extract the profile of the relative magnetization $Z(x) = [n_\uparrow(x) - n_\downarrow(x)]/[n_\uparrow(x) + n_\downarrow(x)]$.

The coupled two-component system can be studied by separately treating the total density ($n = n_\uparrow + n_\downarrow$) and the spin ($n_\uparrow - n_\downarrow = nZ$) degrees of freedom. While the density is simply dominated by a continuity equation, the spin degree of freedom is ruled by a magnetic mean-field Hamiltonian, which has a first-order phase transition in the central region of the cloud for $\Omega_R < |\kappa|n$, where $\kappa \propto \Delta a$ is the relevant interaction parameter (Methods).

The first-order phase transition originates from a symmetry breaking when the local energy landscape as a function of the magnetization Z goes from a single to a double minimum at $\Omega_R = |\kappa|n = 2\pi \times 1{,}150$ Hz in the centre of the cloud. At fixed Ω_R, the experimentally tunable parameter is the detuning δ between the two-level system and the coupling radiation. For small enough $|\delta|$, in the local density approximation (LDA) and in the centre of the trap, the energy landscape $E(Z)$ is represented by an asymmetric double well, which becomes symmetric for $\delta = 0$ (Fig. 2a). In particular, for positive δ, the energy is minimized by positive values of Z, and vice versa.

The double-well scenario is maintained also when the spatial dependence of the field and the bubble interface energy are included. Here, the relevant parameter for the bubble nucleation is the shape (height and width) of the global energy barrier separating the two wells that the system needs to overcome as a field, that is, in a macroscopic manner. This depends on δ, n and Ω_R. When $|\delta|$ exceeds a critical value δ_c, the metastable well disappears[28]. Borrowing the nomenclature from ferromagnetism, $\pm\delta_c$ correspond to the edges of the hysteresis region and their value depends on both Ω_R and $|\kappa|n$.

Figure 2b illustrates the experimental protocol. A coherent coupling with strength Ω_R and initial detuning $\delta_i/2\pi = 5.5$ kHz is switched on. While keeping Ω_R fixed, the detuning δ is linearly changed from δ_i to a variable δ_f at a constant rate of 50 Hz ms^{-1}, by ramping the externally applied magnetic field. Since the ramp starts with $\delta \gg \Omega_R$, the system follows the spin rotation by remaining in the local ground state until $\delta < 0$, when such a local ground state becomes a metastable state (Fig. 2a). Once δ_f is reached and after a variable waiting time t, the states are independently imaged.

If $\delta_f > 0$, the whole system is and remains in the absolute ground state $|\uparrow\rangle$, whereas for $\delta_f < 0$, after a variable time, a macroscopic region

https://doi.org/10.1038/s41567-023-02345-4

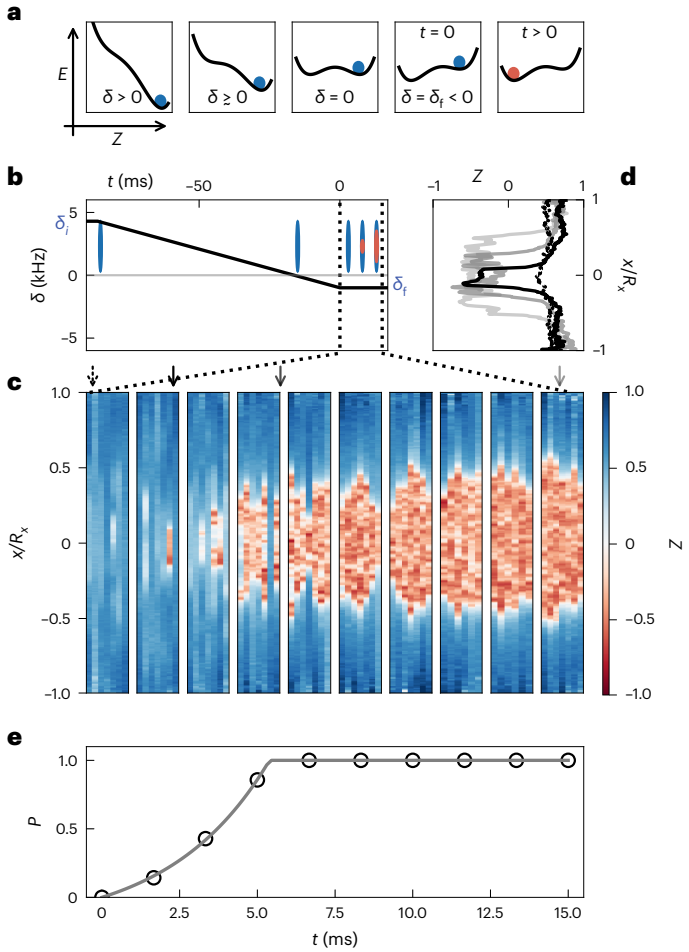

Fig. 2 | Protocols and bubble observation. a, Diagrammatic representations of the local spin energy in the centre of the cloud as a function of the magnetization Z. The first four diagrams correspond to different points across the ramp on δ, whereas the last two compare the initial condition at the end of the ramp and the condition after a waiting time t. The system is initially prepared in the $|\uparrow\rangle$ state. As δ decreases, a second minimum appears, and at $\delta < 0$, the system is in the metastable state, eventually tunnelling across the barrier. **b**, Time variation of δ during the experimental protocol. Ellipses illustrate the cloud spatial magnetization at different t. **c**, Collection of integrated magnetization profiles $Z(x)$ after different waiting times t. For each value of t, up to seven different realizations are shown. **d**, Magnetization profiles for the realizations marked with arrows in **c**. **e**, Measured probability P (empty circles) of observing a shot with a bubble at fixed time. The probability is fitted well with an exponential curve (grey continuous line) until it saturates to 1.

in the central part of the system flips to $|\downarrow\rangle$, generating a bubble; see the examples in Fig. 2c and the magnetization profiles in Fig. 2d. On average, the probability of the occurrence of a bubble is higher if the waiting time is longer (Fig. 2c,e). For a quantitative analysis, at each t, we repeat the measurement up to ten times to investigate the statistical formation of bubbles. Note that, although in uniform systems the bubbles would stochastically nucleate in random spatial positions, the nonuniform density profile of the atomic sample strongly favours the nucleation at the centre of the cloud, where δ_f is closest to δ_c.

A useful quantity for characterizing the bubble nucleation in time is $F_t = (\langle Z\rangle_t - Z_{TV})/(\langle Z\rangle_0 - Z_{TV})$, which was used in ref. 5 to compare an exact diagonalization approach in a zero-temperature spin chain to instanton predictions. Here $\langle Z\rangle_t$ stands for Z measured at time t and averaged over many realizations, Z_{TV} is the magnetization of the true vacuum (TV) state and $\langle Z\rangle_0$ is the initial magnetization of the FV state.

In Fig. 3a,b, we show the average magnetization $\langle Z\rangle_t$ as a function of waiting time for two values of detuning. As the bubble appears always in the centre of the system, to compute F_t, we extract $\langle Z\rangle_t$ in the central 20-μm-wide region ($\approx R_x/10$). The resulting F_t, plotted in Fig. 3c, initially remains flat, and then it exponentially decays because of bubble nucleation. Both features are universal and have been observed in single-particle tunnelling[25,30], quantum field theory[31] and numerical simulations of spin chains[5]. The measured F_t is described well by the empirical function $(1-\epsilon)/\sqrt{1+(e^{t/\tau}-1)^2}+\epsilon$, which is 1 for $t = 0$, scales as t^2 for small t and exponentially decays to ϵ for large t. The two fitting parameters are τ, which describes the characteristic timescale for bubble formation, and ϵ, which takes into account that the asymptotic magnetization $\langle Z\rangle_\infty$ can be different from that of the ground state, Z_{TV} ($F_t = 0$). Note that the timescale τ is related to the exponential decay, whereas the empirical formula takes into account the presence of an initial plateau (in Methods, we show that the plateau length and τ are strictly connected).

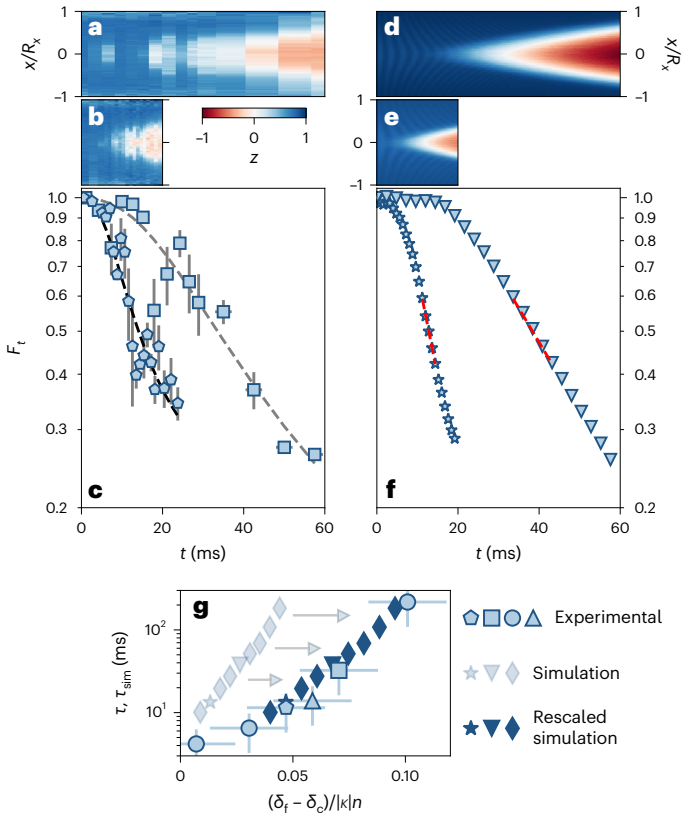

Fig. 3 | Measurement of the bubble formation timescale. a,**b**, Evolution of $\langle Z(x)\rangle$ in time after the ramp on δ for $\Omega_R/2\pi = 300$ Hz, with $\delta_i/\Omega_R = -1.70$ (**a**) and -1.79 (**b**). **c**, Values of F_t evaluated in the 20 μm central region of the cloud are fitted by the empirical expression reported in the text, with squares for the data in **a** and pentagons for the data in **b**. Error bars are the standard deviation for up to ten repetitions. **d**,**e**, Numerical simulations for $\delta_i/\Omega_R = -1.52$ (**d**) and -1.585 (**e**) (before δ_f mapping, see text). **f**, Value of F_t for the simulations, with triangles for the data in **d** and stars for the data in **e**. The red dashed lines are linear fits of the exponentially decaying part. **g**, Experimental τ and numerical τ_{sim} timescale of the bubble formation as a function of $(\delta_f - \delta_c)/|\kappa|n$ extracted from the fit explained in the text. Error bars include statistical uncertainties for the fit and the uncertainty on $(\delta_f - \delta_c)$, which is due to the magnetic field stability and calibration. Numerical timescale of the bubble formation τ_{sim} is shown before (light symbols) and after (dark symbols) rescaling of $(\delta_f - \delta_c)/|\kappa|n$; see the text. The empty triangle is an experimental point taken with a preparation ramp twice as slow as the others to verify the limited impact on the nucleation time resulting from a residual non-adiabaticity in the preparation of the sample.

https://doi.org/10.1038/s41567-023-02345-4

Although the coherent matter field describing the superfluid has a purely quantum origin, at sufficiently high temperatures, quantum fluctuations are dominated by thermal ones, so the dynamics is described well by a mean-field theory based on a classical field description[32]. Numerical simulations based on 1D Gross–Pitaevskii equations (GPEs), reported in Fig. 3d,e, qualitatively reproduce the experimental observations. In the numerics, classical noise is included to simulate the effect of a finite temperature (more details can be found in Methods). The data in Fig. 3d,e were obtained by averaging over 1,000 different realizations of the real-time dynamics in the presence of noise. The large statistics allows us to directly extract the exponential decay time $\tau_{\rm sim}$ through a linear fit of $\ln(F_t)$.

Figure 3g shows six experimental values of τ obtained for $\Omega_{\rm R}/2\pi = 300$ Hz, plotted as a function of the distance from the critical detuning, $(\delta_{\rm f} - \delta_{\rm c})/|\kappa|n$. The results show an exponential dependence on the tuning parameter over two orders of magnitude, from a few to hundreds of milliseconds. Such a sensitivity to a parameter is remarkable for experiments with ultracold atoms. In particular, the experimental observation of the quasi-exponential dependence of τ with respect to $\delta_{\rm f}$ in an interval of the order of 100 Hz critically relies on the magnetic field stability being better than a few tens of microgauss[33].

The values of $\tau_{\rm sim}$ from the simulations (light symbols in Fig. 3g) qualitatively show the same behaviour as the experimental data. The agreement becomes even quantitative (dark symbols in Fig. 3g) when an improved effective 1D description is used, as introduced in ref. 28. This amounts to replacing $(\delta_{\rm f} - \delta_{\rm c})/|\kappa|n$ with $(\delta_{\rm f} - \delta_{\rm c} + c_\delta)/c_\kappa|\kappa|n$ in terms of a small shift $c_\delta/2\pi = 19$ Hz of the critical point and introducing a rescaling factor $c_\kappa = 0.64$ for the interaction energy. This is shown in Fig. 4, which compares the experimental τ and numerical $\tau_{\rm sim}$ for four different values of $\Omega_{\rm R}$, using the same mapping for all simulations in the four panels. Notably, the mapping leads to a remarkable quantitative match between experiment and simulations for all $\Omega_{\rm R}$.

Our observations are consistent with the scenario of a condensate spinor field initially in a ferromagnetic metastable state that decays due to the formation of bubbles (domains) of the ferromagnetic ground state. This mechanism of escaping from the FV finds a suitable theoretical description in terms of an instanton, or critical solution to the field equations in imaginary time[9–11]. Such a theory provides a threshold energy scale $k_{\rm B}T^* = \hbar|\kappa|n \approx k_{\rm B} \times 50$ nK (being $k_{\rm B}$ the Boltzman constant and T^* an effective spin temperature), below (above) which bubbles are nucleated by quantum (thermal) fluctuations. Clearly, the metastability of the FV requires that the energy of the system is smaller than the energy barrier associated with the ferromagnetic interactions and the kinetic energy carried by the bubble domain walls. We estimate such an energy barrier from GPE simulations and find it to be of order of tens of microkelvin.

Within the instanton approach, the bubble nucleation probability has the characteristic timescale:

$$\tau = (\beta E_{\rm c})^{-1/2} A\, {\rm e}^{\beta E_{\rm c}}, \tag{1}$$

which grows exponentially with the energy of the critical solution $E_{\rm c}(\delta, \kappa n, \Omega_{\rm R})$, a quantity that depends on the shape of the many-body potential (Fig. 1). The prefactor depends on fluctuations around the critical solution, but there are very few models for which this factor is calculable, at present. Following the approach of ref. 11, the parameter β is related to the strength of the fluctuations that populate the spin excitation spectrum and trigger bubble formation. For a system in equilibrium at temperature T, one would naturally have $\beta = 1/(k_{\rm B}T)$. In our experiment, however, the system is brought far from thermal equilibrium by the preliminary preparation steps. As such, the strength of its (classical) fluctuations may depend on the details of the preparation protocols and, in particular, on the value of the parameters $\Omega_{\rm R}$ and $(\delta_{\rm f} - \delta_{\rm c})$. Therefore, we regard β and the prefactor A as fitting parameters in the following analysis.

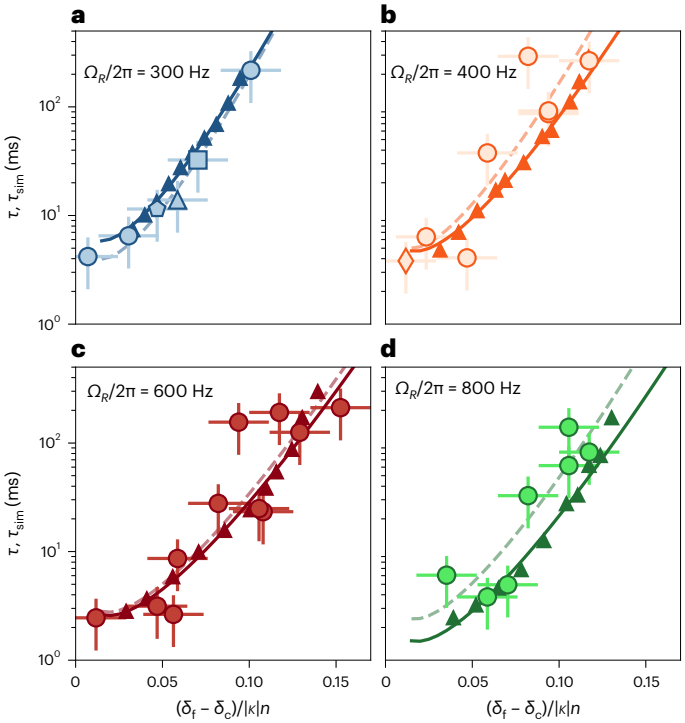

Fig. 4 | Decay times and instanton theory. a–d, Experimental τ and $\tau_{\rm sim}$ from simulations are obtained as explained in the text for $\Omega_{\rm R}/2\pi = 300$ Hz (**a**), 400 Hz (**b**), 600 Hz (**c**) and 800 Hz (**d**). A mapping common to all $\Omega_{\rm R}$ is applied to the horizontal axes of the simulations; see the text. Dashed and full curves are fits of the experimental and simulation data according to the instanton formula. Full markers are for simulation results whereas empty markers are experimental data. Error bars include statistical uncertainties for the fits and the uncertainty of $\delta_{\rm f}$ due to the magnetic field stability.

We can estimate $E_{\rm c}$ within the instanton theory, and provide an analytical expression in the limit of vanishing energy barrier (small $\delta_{\rm f} - \delta_{\rm c}$), by considering a homogeneous 1D system described only by the scalar field Z. The potential for the magnetization field Z can be written[28] as

$$V(Z) = -\hbar\left(|\kappa|nZ^2 + 2\Omega_{\rm R}\sqrt{1-Z^2} + 2\delta_{\rm f}Z\right), \tag{2}$$

and the instanton energy, in units of the interaction energy, reads

$$\frac{E_{\rm c}}{\hbar|\kappa|n} = \sqrt{\frac{\hbar n}{2m|\kappa|}}\int_{Z_{\rm TP}}^{Z_{\rm FV}}\left[\frac{V(Z) - V(Z_{\rm FV})}{\hbar|\kappa|n(1-Z^2)}\right]^{1/2}{\rm d}Z, \tag{3}$$

where $Z_{\rm TP}$ is the classical turning point (in the inverted potential $-V$) and $Z_{\rm FV}$ the value of the magnetization of the metastable state. Most of our data are taken in a regime where the height of the barrier is much smaller than the depth of the ground state well (in the tens of millikelvin range). In this limiting case, $E_{\rm c}$ depends (Methods) on $\Omega_{\rm R}$ and $(\delta_{\rm f} - \delta_{\rm c})$ as

$$E_{\rm c} \propto \left(\frac{\delta_{\rm f} - \delta_{\rm c}}{|\kappa|n}\right)^{5/4}\left(\frac{\Omega_{\rm R}}{|\kappa|n}\right)^{1/6}\left(\frac{|\delta_{\rm c}|}{|\kappa|n}\right)^{-1/4}. \tag{4}$$

For each value of $\Omega_{\rm R}$, we fit both experimental and numerical data to equation (1) using A and β as free parameters with $E_{\rm c}$ given by equation (4), see values in Table 1. As shown in Fig. 4, the dependence on $(\delta_{\rm f} - \delta_{\rm c})^{5/4}$ is well caught by the instanton model, which is the key feature supporting the instanton interpretation. The β value and the prefactor A decrease for increasing $\Omega_{\rm R}$, and further theoretical and experimental investigations are needed to explain this dependence (Methods). As an a posteriori consistency check, we have verified that the value of the effective temperatures associated with the fitted β

indeed fall below the barrier height parameter E_c and above the quantum limit T^*. Still, keeping in mind the approximations made to derive equation (4)—in particular the absence of the trapping potential, the absence of a relative phase and density fluctuations and the small barrier limit—the agreement among experiment, simulation and instanton theory is remarkable. The instanton theory appears to capture the main dependence of the FV decay rate on the microscopic parameter δ_f, which is responsible for the broken $\mathbb{Z}_2$ symmetry.

In this paper, we present solid evidence of the thermally induced macroscopic tunnelling of a coherent matter field, manifested by bubbles of a TV phase nucleating in a FV state. The false and true vacua are the local and global energy minima of a ferromagnetic atomic Bose–Einstein condensate, respectively. The experimental results suggest a dominant exponential dependence of the decay rate on the effective energy barrier, which, itself, depends on the distance from the critical point of the ferromagnetic transition. Such a dependence is successfully captured by numerical simulations of the classical field dynamics, as well as by a simple instanton theory based on a reduced energy functional for the magnetization.

Our experimental platform paves the way to exploring the process of bubble formation and growth in intricate detail and to building a new bridge between low-energy and high-energy phenomena characterized by metastability within a first-order phase transition. In this spirit, our work opens up new avenues in the understanding of the early Universe as well as ferromagnetic quantum phase transitions. The possibility of engineering the barrier properties through the injection of tailored noise and of deterministically seeding bubbles are promising future directions for experimental investigations with a focus on the role of dissipation, the existence of a shortcut to adiabaticity[34,35], the creation of entanglement and domain-wall confinement[36], coupling with the environment[37], and relativistic and nonrelativistic aspects of bubble nucleation and dynamics. Furthermore, experimental efforts towards colder systems would allow us to reach a quantum tunnelling regime where the bubble nucleation process is dominated by quantum fluctuations of the field. A natural extension of the present work is for a dimensionality larger than 1, for which the theoretical treatment is challenging.

Online content

Any methods, additional references, Nature Portfolio reporting summaries, source data, extended data, supplementary information, acknowledgements, peer review information; details of author contributions and competing interests; and statements of data and code availability are available at https://doi.org/10.1038/s41567-023-02345-4.

References

1. Hogan, C. Gravitational radiation from cosmological phase transitions. *Mon. Not. R. Astron. Soc.* **218**, 629 (1986).
2. Shaposhnikov, M. E. Baryon asymmetry of the Universe in standard electroweak theory. *Nucl. Phys. B* **287**, 757 (1987).
3. Feeney, S. M., Johnson, M. C., Mortlock, D. J. & Peiris, H. V. First observational tests of eternal inflation: analysis methods and WMAP 7-year results. *Phys. Rev. D* **84**, 043507 (2011).
4. Sinha, A., Chanda, T. & Dziarmaga, J. Nonadiabatic dynamics across a first-order quantum phase transition: quantized bubble nucleation. *Phys. Rev. B* **103**, L220302 (2021).
5. Lagnese, G., Surace, F. M., Kormos, M. & Calabrese, P. False vacuum decay in quantum spin chains. *Phys. Rev. B* **104**, L201106 (2021).
6. Milsted, A., Liu, J., Preskill, J. & Vidal, G. Collisions of false-vacuum bubble walls in a quantum spin chain. *PRX Quantum* **3**, 020316 (2022).
7. Baldwin, A. J. et al. Metastability of native proteins and the phenomenon of amyloid formation. *J. Am. Chem. Soc.* **133**, 14160 (2011).
8. Ghosh, D. & Ranjan, A. The metastable states of protein. *Protein Sci.* **29**, 1559 (2020).
9. Coleman, S. R. The fate of the false vacuum. 1. Semiclassical theory. *Phys. Rev. D* **15**, 2929 (1977); erratum **16**, 1248 (1977).
10. Callan, C. G. & Coleman, S. R. The fate of the false vacuum. 2. First quantum corrections. *Phys. Rev. D* **16**, 1762 (1977).
11. Linde, A. D. Decay of the false vacuum at finite temperature. *Nucl. Phys. B* **216**, 421 (1983); erratum **223**, 544 (1983).
12. Mazumdar, A. & White, G. Review of cosmic phase transitions: their significance and experimental signatures. *Rept. Prog. Phys.* **82**, 076901 (2019).
13. Hindmarsh, M., Lüben, M., Lumma, J. & Pauly, M. Phase transitions in the early Universe. *SciPost Phys. Lect. Notes* https://doi.org/10.21468/SciPostPhysLectNotes.24 (2021).
14. Devoto, F., Devoto, S., Di Luzio, L. & Ridolfi, G. False vacuum decay: an introductory review. *J. Phys. G, Nucl. Part. Phys.* **49**, 103001 (2022).
15. Fialko, O., Opanchuk, B., Sidorov, A. I., Drummond, P. D. & Brand, J. Fate of the false vacuum: towards realization with ultra-cold atoms. *Europhys. Lett.* **110**, 56001 (2015).
16. Braden, J., Johnson, M. C., Peiris, H. V. & Weinfurtner, S. Towards the cold atom analog false vacuum. *J. High Energy Phys.* **2018**, 14 (2019).
17. Billam, T. P., Gregory, R., Michel, F. & Moss, I. G. Simulating seeded vacuum decay in a cold atom system. *Phys. Rev. D* **100**, 065016 (2019).
18. Davoudi, Z. et al. Towards analog quantum simulations of lattice gauge theories with trapped ions. *Phys. Rev. Res.* **2**, 023015 (2020).
19. Billam, T. P., Brown, K. & Moss, I. G. Simulating cosmological supercooling with a cold-atom system. *Phys. Rev. A* **102**, 043324 (2020).
20. Billam, T. P., Brown, K., Groszek, A. J. & Moss, I. G. Simulating cosmological supercooling with a cold atom system. II. Thermal damping and parametric instability. *Phys. Rev. A* **104**, 053309 (2021).
21. Ng, K. L., Opanchuk, B., Thenabadu, M., Reid, M. & Drummond, P. D. Fate of the false vacuum: finite temperature, entropy, and topological phase in quantum simulations of the early Universe. *PRX Quantum* **2**, 010350 (2021).
22. Song, B. et al. Realizing discontinuous quantum phase transitions in a strongly correlated driven optical lattice. *Nat. Phys.* **18**, 259–264 (2022).
23. Preskill, J. Simulating quantum field theory with a quantum computer. In *Proceedings of The 36th Annual International Symposium on Lattice Field Theory—PoS(LATTICE2018)*. 24 (Sissa Medialab, 2019).
24. Abel, S. & Spannowsky, M. Quantum-field-theoretic simulation platform for observing the fate of the false vacuum. *PRX Quantum* **2**, 010349 (2021).
25. Kramers, H. Brownian motion in a field of force and the diffusion model of chemical reactions. *Physica* **7**, 284 (1940).
26. Grabert, H. & Weiss, U. Crossover from thermal hopping to quantum tunneling. *Phys. Rev. Lett.* **53**, 1787 (1984).
27. Grabert, H., Weiss, U. & Hanggi, P. Quantum tunneling in dissipative systems at finite temperatures. *Phys. Rev. Lett.* **52**, 2193 (1984).
28. Cominotti, R. et al. Ferromagnetism in an extended coherently coupled atomic superfluid. *Phys. Rev. X* **13**, 021037 (2023).
29. Farolfi, A. et al. Manipulation of an elongated internal Josephson junction of bosonic atoms. *Phys. Rev. A* **104**, 023326 (2021).
30. Hänggi, P., Talkner, P. & Borkovec, M. Reaction-rate theory: fifty years after Kramers. *Rev. Mod. Phys.* **62**, 251 (1990).
31. Szász-Schagrin, D. & Takács, G. False vacuum decay in the (1+1)-dimensional φ^4 theory. *Phys. Rev. D* **106**, 025008 (2022).

32. Sinatra, A., Castin, Y., Carusotto, I., Lobo, C. & Witkowska, E. in *Quantum Gases* (eds Proukakis, N., Gardiner, S., Davis, M. & Szymańska, M.) 215–228 (World Scientific, 2013); https://doi.org/10.1142/9781848168121_0014
33. Farolfi, A. et al. Design and characterization of a compact magnetic shield for ultracold atomic gas experiments. *Rev. Sci. Instrum.* **90**, 115114 (2019).
34. Guéry-Odelin, D. et al. Shortcuts to adiabaticity: concepts, methods, and applications. *Rev. Mod. Phys.* **91**, 045001 (2019).
35. Torrontegui, E. et al. in *Advances in Atomic, Molecular, and Optical Physics*, Vol. 62 (eds Arimondo, E., Berman, P. R. & Lin., C. C.) Ch. 2 (Academic, 2013).
36. Tan, W. L. et al. Domain-wall confinement and dynamics in a quantum simulator. *Nat. Phys.* **17**, 742–747 (2021).
37. Maki, J. A., Berti, A., Carusotto, I. & Biella, A. Monte Carlo matrix-product-state approach to the false vacuum decay in the monitored quantum Ising chain. *SciPost Phys.* **15**, 152 (2023).

Methods

Ferromagnetism in elongated mixtures

The ferromagnetic properties of atomic superfluid coupled mixtures are experimentally measured and discussed in ref. 28. Here we summarize the key ingredients to help in understanding the results presented in the main text of the article.

Our system is composed of two sodium hyperfine states $|F, m_F\rangle = |2, -2\rangle \equiv |\uparrow\rangle$ and $|1, -1\rangle \equiv |\downarrow\rangle$, where F is the total angular momentum and m_F its projection. The two populations, $n_\uparrow(x, y)$ and $n_\downarrow(x, y)$, are independently measured by shadow imaging. Starting from the 2 two-dimensional pictures of the cloud, we determine the relative magnetization $Z(x) = [n_\uparrow(x) - n_\downarrow(x)]/n(x)$, where $n_{\uparrow,(\downarrow)}(x) = \int n_{\uparrow,(\downarrow)}(x, y)\, dy$ and $n(x) = \int [n_\uparrow(x, y) + n_\downarrow(x, y)]\, dy$ are the 1D integrated densities. The integration along y takes advantage of the suppressed radial dynamics. In the LDA, the energy per particle associated with the spin channel of the mixture is

$$E(Z, \phi) \propto -|\kappa| n Z^2 - 2\Omega_R \sqrt{1 - Z^2} \cos\phi - 2\delta_f Z, \tag{5}$$

where the phase ϕ is the relative phase between $|\uparrow\rangle$ and $|\downarrow\rangle$. The detuning δ_f used in the text is equal to $\delta_B + n\Delta$, where δ_B is experimentally tunable by changing the applied magnetic field and consequently the Zeeman splitting between the two states. The quantities κ and Δ are associated with the collisional proprieties of the mixture and are

$$\Delta \equiv \frac{g_{\downarrow\downarrow} - g_{\uparrow\uparrow}}{2\hbar} < 0, \tag{6}$$

$$\kappa \equiv \frac{g_{\downarrow\downarrow} + g_{\uparrow\uparrow}}{2\hbar} - \frac{g_{\downarrow\uparrow}}{\hbar} < 0, \tag{7}$$

where $g_{\downarrow\downarrow}$, $g_{\uparrow\uparrow}$ and $g_{\downarrow\uparrow}$ are the two intracomponent and the intercomponent interaction constants. Note that $n\Delta$ derives from the $|\uparrow\rangle$ and $|\downarrow\rangle$ self-interaction asymmetry ($g_{\uparrow\uparrow} \neq g_{\downarrow\downarrow}$).

In an elongated cloud having a parabolic Thomas–Fermi density profile, the ferromagnetic phase is in the centre of the cloud where the nonlinear term $|\kappa| n Z^2$ is maximal. Under the condition $|\kappa| n > \Omega_R$, in fact, the energy per particle is characterized by a symmetric double-well structure, which is a signature of the symmetry breaking and is typical of the ferromagnetic phase. At non-zero detuning, the symmetry of the two wells is broken. Thanks to the tuning knob δ_B, one can change the relative energy difference between the two energy minima, converting one or the other state into the absolute ground state or the metastable state. Given their smaller density, the tails of the cloud remain in the paramagnetic regime and the relative magnetization Z of the single energy minimum is unambiguously determined by δ_B.

Due to the asymmetry between $|\uparrow\rangle$ and $|\downarrow\rangle$, there exists a range of values of δ_B for which the sign of Z at the energy minima in the centre (−) and at the tails (+) is opposite, but the system can still maintain a homogeneous positively magnetized profile being metastable in the centre. When the detuning is decreased below the critical value δ_c (see main text), the metastable minimum disappears, resulting in a unique steady magnetic profile with negative Z in the centre and positive Z in the tails.

Although the spin energy profiles of equation (5) are useful for explaining the presence of two distinguished minima, this LDA representation shows only the LDA energy landscape per particle and not the total energy of the system. For instance, the LDA energy profiles do not include the kinetic energy contribution arising from the nonuniform magnetization. At the domain walls of a bubble, in fact, Z changes spatially within a length that depends on $|\kappa| n/\Omega_R$. The energy barrier in Fig. 1, instead, is intended to include also this kinetic energy contribution.

Calibration and analysis procedure

An important calibration concerns the determination of the critical detuning at which the double-well energy landscape is expected to disappear. We determine δ_c with the protocol used in ref. 28 to measure the hysteresis width of the ferromagnetic regime. This is based on the same ramp shown in Fig. 2b, applied with a null waiting time.

The data used in the main text are obtained in the range of δ_f directly above the critical value. Since the bubble appears in the central region of the cloud, we focus on the central 40 μm and set a threshold on the average magnetization, $Z_{bubble} = 0.2$, below which we count the presence of the bubble. The total bubble counts at fixed waiting time determine the probability P plotted in Fig. 2e. We verify that the choice of the threshold Z_{bubble} and the averaging area do not critically impact the outcomes presented here. Once the bubble is detected, the full magnetization profile is initially fitted with a double sigmoidal function:

$$C\left[\arctan\left(\frac{x - x_r}{s_r}\right) - \arctan\left(\frac{x - x_l}{s_l}\right)\right], \tag{8}$$

where C is the amplitude and $x_{(r),[l]}$ and $s_{(r),[l]}$ are the (right) [left] centres and sigmas of the two sigmoids. The positions $x_{(l),[r]}$ are then used as starting values for a second fitting routine that independently analyses the left and right bubble interfaces. This second step is used to better determine the exact positions of the interfaces without the effects of cloud asymmetry and offsets. The obtained values $x_{(l),[r]}$ allow us to determine the bubble size as $\sigma_x = x_r - x_l$.

Determination of the decay time

In the main text, we explain how we determine the characteristic decay time τ by fitting F_t to $(1 - \epsilon)/\sqrt{1 + (e^{t/\tau} - 1)^2} + \epsilon$. This formula allows us to extract τ, even for experimental sequences with limited statistics, and it is robust against the initialization of the fitting parameters.

To verify the solidity of our approach, we also considered a different characteristic time $\tau_{50\%}$, defined as the time at which the probability P of observing a bubble is 50%. This approach is a valid alternative for measurements featuring limited statistics. To determine $\tau_{50\%}$, we fit P with the following function:

$$P(t) = \min\left[a_1(e^{t/a_2} - 1), 1\right], \tag{9}$$

with a_1 and a_2 as free parameters. These two are then used to determine $\tau_{50\%}$ from

$$\frac{1}{2} = a_1\left(e^{t_{50\%}/a_2} - 1\right). \tag{10}$$

We checked, within the statistical uncertainties, that the value of $\tau_{50\%}$ is rather insensitive to the choice of the fitting function (linear or exponential with offsets in time and P). Extended Data Fig. 1 shows that τ and $\tau_{50\%}$ are compatible, both for the experimental measurements and for the numerical simulations. In particular, the simulation results allow us to conclude that, although $\tau_{50\%}$ is expected to be influenced by the delay time before the bubble decays, $\tau_{50\%}$ is still a good approximation of τ. This suggests that the delay time and τ are related, and further investigations are necessary to understand how.

In general, we conclude that the determination of τ used in the main text is solid. In particular, note that the two methods rely on two very different observables, the mean magnetization in the centre, averaged over all experimental shots (τ), and the probabilistic presence of a bubble ($\tau_{50\%}$).

Numerical simulations

The numerical results presented in the main text are based on 1D Gross–Pitaevskii simulations. The parameters are chosen to faithfully reproduce the experimental conditions: in particular, the system trapped by a harmonic potential with frequency $\omega_0 \approx 2\pi \times 16$ Hz, so that the Thomas–Fermi radius is $L \approx 200$ μm. Moreover, the interactions are chosen to obtain $|\kappa| n = |\Delta| n \approx 2\pi \times 1.1$ kHz, n being the total density in the centre of the cloud. The system is first prepared through an imaginary-time evolution in the ground state corresponding to

$\delta_i = 2\pi \times 1$ kHz. Thus, regardless of the value of Ω_R, it is almost fully polarized in the $|\uparrow\rangle$ state.

To simulate the finite temperature of the initial state, white noise with an amplitude equal to 6% of the total density is added on top of the ground state. This corresponds to an injected energy of roughly $\varepsilon \approx 0.6|\kappa|n$ per particle. We then let the system evolve in real time, without changing any parameter, and we observe that, after a transient, the noise distribution becomes stationary. We interpret this result as the thermalization of the mixture to a temperature $T \propto \varepsilon$. Under an ergodicity assumption, we can determine the following dynamics of the system by averaging over many repetitions of the same time evolution, each one obtained starting from a different noisy sample. To summarize, we perform mean-field simulations in which noise plays the role of an effective temperature. Of course, these do not allow us to investigate the role of quantum fluctuations. However, since the estimated experimental temperature is much higher than $|\kappa|n_0/k_B \approx 50$ nK, the dynamics is likely to be dominated by thermal noise so that a comparison with classical field simulations is justified.

The real-time dynamics after thermalization is built to reproduce the experimental protocol. A detuning ramp with speed 50 Hz ms^{-1} is applied to reach the FV state corresponding to some final $\delta_f < 0$. The magnetization of the system is then monitored after a variable waiting time in the range [10, 300] ms, depending on the simulation parameters.

To extract the characteristic decay times τ and τ_{50}, we compute:

$$F_t = \frac{\langle Z(x \approx 0, t)\rangle - Z_{TV}}{\langle Z\rangle_0 - Z_{TV}}, \tag{11}$$

where $\langle Z(x \approx 0, t)\rangle$ is the statistical average of magnetization over the central 10 μm of the cloud and $\langle Z\rangle_0$ in the simulation is identical to Z_{FV}. If the number of samples is sufficiently high (we use 1,000), this function represents the probability of not observing a bubble at time t. Therefore, $\tau_{50\%}$ is computed, by definition, by solving $F_{\tau_{50\%}} = 0.5$.

FV decay rates are obtained instead from a linear fit of $\log F_t$. In most cases, the predicted exponential behaviour is found within a time interval corresponding to $F_t \in [0.3, 0.7]$. Small adjustments of this window are necessary for simulations with the shortest and longest tunnelling times.

Instantons

The theoretical description of the vacuum decay process requires a non-perturbative description of the field dynamics, for instance based on instanton solutions to the equations of motion using an imaginary-time coordinate. The classical field theory for this system reduces down to a field theory for the magnetization Z. For thermal instantons in one dimension, bubbles are expected to nucleate with a characteristic time (see, for example, ref. 13):

$$\tau = A(\beta E_c)^{-1/2} e^{\beta E_c}, \tag{12}$$

where $\beta = 1/(k_B T)$ and E_c is the energy of the instanton and the factor A depends on the fluctuations around the instanton solution. As there are a very limited number of models for which the prefactor A is calculable at present, we will regard A as a fitting parameter in the subsequent analysis. Note that this non-perturbative approach based on instantons is valid only when the exponent is larger than 1, that is, for temperatures $k_B T < E_c$. At even lower temperatures, vacuum fluctuations become the dominant seeding mechanism. In our system, this is expected to happen for $k_B T < \hbar|\kappa|n \approx 50$ nK, and the resulting vacuum decay rate would be far less than the rate seen in the experiment.

The energy for a thermal instanton includes a gradient contribution:

$$E_c = \frac{n}{4}\int\left\{\frac{\hbar^2}{2m}\frac{(\nabla Z)^2}{1-Z^2} + V\right\}dx, \tag{13}$$

Table 1 | Fitting coefficients for the thermal instanton model of vacuum decay

$\Omega_R/2\pi$	A_{exp}	b_{exp}	$T_{eff,exp}$ [μK]	A_{sim}	b_{sim}	$T_{eff,sim}$
300	1.6(2)	56(2)	2.8(1)	2.5(2)	55(1)	2.8(1)
400	2(1)	48(8)	3.3(5)	2.0(4)	41(1)	3.8(1)
600	1.2(6)	31(4)	5(7)	1.1(1)	30(1)	5.2(2)
800	1.0(6)	28(5)	5.6(9)	0.67(7)	25(1)	6.2(3)

The fit is limited to $(\delta_f - \delta_c)/|\kappa n| > 0.03$ to ensure that $b\hat{E}_c > 1$. The table contains the fitting coefficients for the four different coupling frequencies for experimental data and simulations.

where V is the potential as in equation (2). We can scale out the dependence on the density so that $\hat{E}_c = E_c/(\hbar n^2 \xi|\kappa|)$ for the length scale $\xi = \sqrt{\hbar/(m|\kappa|n)}$. For thermal bubbles in one dimension, the instanton calculation is equivalent to a WKB approximation to the action, with the familiar WKB form:

$$\hat{E}_c = \frac{1}{2}\int_{Z_{TP}}^{Z_{FV}}\left(\frac{2(V - V_{FV})}{\hbar|\kappa|n}\right)^{1/2}\frac{dZ}{\sqrt{1-Z^2}}, \tag{14}$$

The integral extends from the turning point Z_{TP} to the FV Z_{FV}. The extra factor $1/\sqrt{1-Z^2}$ is due to the form of the derivative terms in the energy (equation (13)).

For small potential barriers, the potential can be expanded to cubic order about an inflection point at Z_c and $\delta = \delta_c$, where

$$\delta_c = -|\kappa|nZ_c^3, \qquad Z_c = \left(1 - \left(\frac{\Omega_R}{|\kappa|n}\right)^{2/3}\right)^{1/2}. \tag{15}$$

The integral in this case can be evaluated exactly:

$$\hat{E}_c \approx 1.77\left(\frac{\delta_f - \delta_c}{|\kappa|n}\right)^{5/4}\left(\frac{\Omega_R}{|\kappa|n}\right)^{1/6}\left(\frac{|\delta_c|}{|\kappa|n}\right)^{-1/4}. \tag{16}$$

Although a precise prediction of the prefactor A is impractical, we follow ref. 13 and use an order of magnitude estimate:

$$A \approx \{V''(Z_{FV})\}^{-1}, \tag{17}$$

where a prime denotes $\sqrt{1-Z^2}\,\partial/\partial Z$. In the same small barrier limit used above:

$$A \approx \left(\frac{\Omega_R}{|\kappa|n}\right)^{-1/3}\left(\frac{\delta_f - \delta_c}{|\kappa|n}\right)^{-1/2}, \tag{18}$$

up to a constant factor. Although the dependence on δ is dominated by the dependence in the exponent of equation (12), equation (18) suggests that A decreases with Ω_R, as also found in the experiment and in the simulations.

The experimental and simulations data have been used to determine the best parameters in a fit for $\ln\tau = \ln A + b\hat{E}_c - \ln(b\hat{E}_c)/2$ at fixed Ω_R. The results for the four different values of Ω_R are given in Table 1. The parameter b decreases as Ω_R increases and values of A and b are compatible within the statistical uncertainties between the experimental data and simulations. The effective temperature $T_{eff,exp[sim]} = (\hbar n^2 \xi|\kappa|)/(k_B b_{exp[sim]})$ can be estimated by using the experimental atomic density $n \approx 4{,}600$ atoms μm^{-1}. The effective temperature increases with Ω_R and power-law fits provide $T_{eff,exp} \propto \Omega_R^{0.76(6)}$ and $T_{eff,sim} \propto \Omega_R^{0.77(12)}$.

To verify that the instanton prediction and the classical field simulations are consistent, we repeated the latter using different values of the initial noise ε at a fixed value of δ_f. We observe that the extracted τ results are proportional to $\exp(1/\varepsilon)$, which justifies the association between the injected noise parameter ε and the temperature T.

Data availability

Data for all figures are provided. Source data are provided with this paper. Two-dimensional raw atomic cloud pictures from all experimental runs are available upon request to A.Z.

Code availability

Analysis codes are available upon request to A.Z.

Acknowledgements

We thank A. Biella, P. Hauke and Y. Castin for fruitful discussions. We acknowledge funding from Provincia Autonoma di Trento, from the National Institute for Nuclear Physics (INFN) through the FISH project, from the Italian Ministry of Education, University and Research under the PRIN2017 project CEnTraL (Protocol Number 20172H2SC4), from the European Union's Horizon 2020 research and innovation programme through the STAQS and DYNAMITE projects of QuantERA II (Grant Agreement No. 101017733), from the European Research Council under the European Union's Horizon 2020 research and innovation programme (Grant Agreement No. 804305), from the UK Quantum Technologies for Fundamental Physics programme (Grant No. ST/W006162/1) and from the PNRR MUR project PE0000023-NQSTI. This work was supported by Q@TN, the joint laboratory between the University of Trento, Fondazione Bruno Kessler, INFN and the National Research Council.

Author contributions

G.F., G.L. and A.Z. conceived the project. R.C., C.R. and A.Z. performed the experiments and analysed the data. A.B., I.C., I.M., T.B. and A.R. performed the theoretical analysis. A.B. developed the numerical code and performed the simulations. G.F. supervised the project. All authors contributed to the discussion and interpretation of the results and paper writing.

Competing interests

The authors declare no competing interests.

Additional information

Extended data Extended data are available for this paper at https://doi.org/10.1038/s41567-023-02345-4.

Correspondence and requests for materials should be addressed to A. Zenesini, G. Lamporesi or A. Recati.

Peer review information *Nature Physics* thanks Sascha Hoinka and the other, anonymous, reviewer(s) for their contribution to the peer review of this work.

https://doi.org/10.1038/s41567-023-02345-4

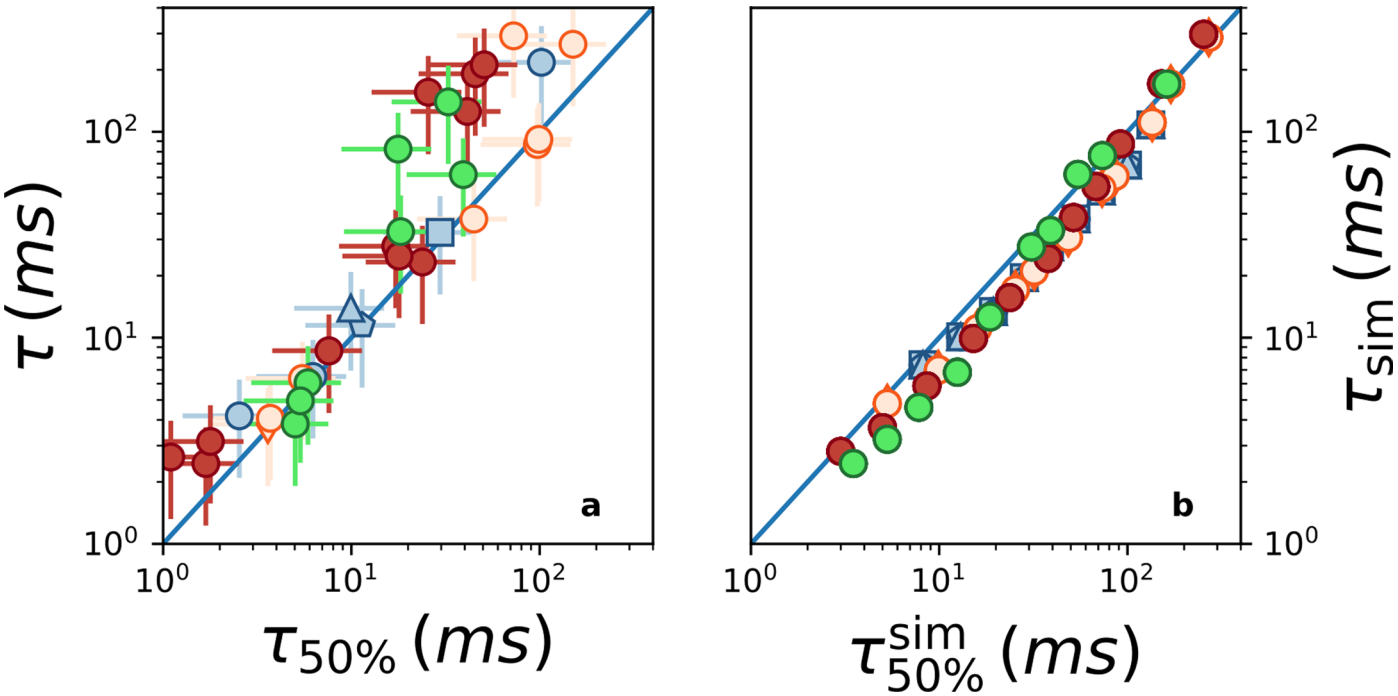

Extended Data Fig. 1 | τ vs $\tau_{50\%}$ for experimental (a) and numerical (b)results. The two quantities are compatible to each other within error bars in experimental results and show only small deviation in simulation data. Color code for the points is the same used in the main text and the blue line marks $tau = \tau_{50\%}$.